# Radiologically Defined Tumor-habitat Adjacency as a Prognostic Biomarker in Glioblastoma

Xuan Xu[1], Dimitris Samaras[1], Prateek Prasanna[2]

*Abstract*— Intratumor heterogeneity in glioblastoma (GBM) has been linked to adverse clinical outcomes including poor survival and sub-optimal response to therapies. Different techniques, such as *radiomics*, have been used to characterize GBM phenotype. However, the spatial diversity and the interaction between different sub-regions within the tumor (habitats) and its microenvironment has been relatively unexplored. Besides, existing approaches have mainly focused on the radiomic analysis within globally defined regions without considering local heterogeneity. In this paper, we developed a 3D spatial co-localization descriptor based on the adjacency of "habitats" to quantify the diversity of physiologically similar sub-regions on multi-protocol magnetic resonance imaging. We demonstrated the utility of this spatial phenotype descriptor in predicting overall patient survival. Our experimental results on N=236 treatment-naïve MRI scans suggest that the co-localization features in conjunction with traditional clinical measures, such as age and tumor volume, outperform texture based radiomic features. The presented descriptor provides a tool for more complete characterization of intratumor heterogeneity in solid cancers.

*Clinical relevance*— Our model demonstrates the significance of spatial co-localization of radiologically defined global and local tumor-habitats in providing early personalized risk prediction and characterizing overall survival in GBM.

## I. INTRODUCTION

Glioblastoma multiforme (GBM) is the most aggressive brain tumor. With treatment including surgical resection, local radiation therapy, and systemic chemotherapy, the median survival of GBM patients is around 12-15 months with only 3-5% patients surviving for more than 3 years [1]. This poor prognosis leads to a need for personal risk prediction approach at an early stage so that treatment may be tailored according to the predicted individual risk profile.

Magnetic Resonance Imaging (MRI) is a key tool in diagnosis and treatment management for GBM patients; different sequences, such as T1, T2, and FLAIR provide complementary phenotypic information. Intratumor heterogeneity, as manifested on multi-protocol MRI (mp-MRI), have been shown to be good indicators of long term survival in GBM [2]. Spatial heterogeneity observed on mp-MRI can be characterized by quantifying the imaging properties of physiologically similar sub-regions or "habitats". This has however been largely limited to radiomic analysis on more globally-defined sub-regions [3], without taking into account local heterogeneity within the different imaging protocols.

[1]Department of Computer Science, Stony Brook University, NY, USA
[2]Department of Biomedical Informatics, Stony Brook University, NY, USA prateek.prasanna@stonybrook.edu

Zhou et al. have previously generated radiologically defined habitats within brain tumor regions to characterize the spatial heterogeneity of the lesions [4]. In this study, a non-parametric Otsu algorithm was leveraged to divide the intratumor habitats from each modality separately [5]. An intersect operation was conducted between two MRI protocols to define the final habitats. The authors further demonstrated that distribution of MRI-defined habitats varies significantly among the different survival groups. Wu et al. [6], separated F-FDG PET and contrast CT imaging by superpixels to define habitats and compared the imaging changes between pre-treatment and mid-treatment timepoints in oropharyngeal squamous cell carcinoma patients. The proposed imaging signature significantly outperformed traditional metrics, such as radiomic features and the change in tumor volume, in predicting progression free survival. Radiomic features of GBM habitats, including shape and texture-based descriptors, have been used in conjunction with prognostic models to characterize overall survival [8]. However, such techniques rely on intensity harmonization across scanners and institutions to ensure robustness and reproducibility.

We hypothesize that adjacency of "habitats" contributes to lesion heterogeneity, leading to abnormal tumor growth and proliferation, and eventually impacts long term outcome. In this work, we quantify the spatial diversity of local and global habitats by constructing region adjacency graphs to extract the inner structural information of tumors on mp-MRI. We further demonstrate the prognostic importance of these habitat metrics in a survival prediction setting. The key contributions of this work are as follows:

- Development of a novel 3D spatial co-localization descriptor to quantify the spatial diversity of physiologically similar sub-regions on mp-MRI.
- Demonstrating the prognostic importance of radiologically defined tumor habitats in characterizing overall survival in GBM.

## II. MATERIALS AND METHODS

### A. Study Population

Multi-protocol treatment-naïve MR images (T1, post-contrast T1-weighted (T1-Gd), T2-weighted, T2 Fluid Attenuated Inversion Recovery(T2-FLAIR)) of 236 GBM patients from the BraTS 2020 training dataset were used in this analysis [9], [11]. The data set included 369 subjects, with corresponding overall survival information (in days post baseline imaging) available for 236 cases. The ground truth
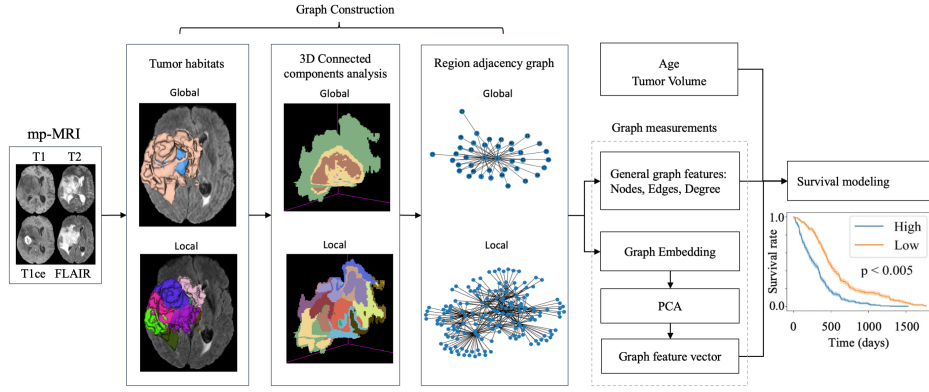
Fig. 1. Overview of workflow comprising habitat identification, graph construction, and survival modeling

tumor segmentation consists of the enhancing tumor (ET), the peritumoral edema (ED), and the necrotic region and non-enhancing tumor core (NCR/NET). The mp-MRI data is co-registered to the same anatomical template, interpolated to the sample resolution of $1mm^3$, and skull-stripped. The clinico-pathologic data also included the age of patients and resection status.

### B. Methods

The overall workflow in presented in Figure 1.

*1) Notations:* Given a tumor segmentation $I_i$ for subject $i$, $C_i = (c_{i1}, c_{i2}, ..., c_{in})$ denotes the 3D connected components within the radiologically defined tumor habitats, where $n$ is the number of connected components, $c_{ij}$ $(j = 1, ..., n)$ denotes the $j^{th}$ connected component. $G_i = (V_i, E_i)$ denotes the region adjacency graph for subject $i$, where $V_i = (v_{i1}, v_{i2}, .., v_{im})$ is the node set, $m$ represents the node number, and $E_i = (e_{i1}, e_{i2}, ..e_{is})$ is the edge set, $s$ represents the number of edges.

*2) Habitat Identification and Graph Construction:* The algorithm is described as follows:

- Segmentation of the tumors into different subcompartments is critical to habitat definition. $Volume_i = (NET_i, ET_i, ED_i)$ is extracted for every subject $i$, where $NET_i$ denotes the number of voxels in NET/NCR, $ET_i$ denotes the number of voxels in ET, and $ED_i$ denotes the number of voxels in ED.
- Habitat identification
  1) Global habitats: The ground truth tumor sub-compartment segmentations are defined as the global habitats, which include the ET, ED, and the NCR/NET regions.
  2) Local habitats: maskSLIC was used to re-segment the tumor into 20 supervoxels based on their intensity distribution in the mp-MRI [12]. 20 local habitats were defined on each of the different MRI protocols using the iterative clustering method.
- For each subject $i$, $C_i = (c_{i1}, c_{i2}, ..., c_{in})$ is calculated based on the global and the local habitats, independently [13]. Two voxels are connected if they share the same label and are adjacent. Since we use 3D MRI, the

connectivity is 26. $C_i = (C_i^{adj}, C_i^{no\_adj})$, where $C_i^{adj}$ denotes the connected component set with neighbors, and $C_i^{no\_adj}$ denotes the connected components without neighbors.

- For each connected component vector $C_i^{adj}$, a region adjacency graph (RAG) $G_i = (V_i, E_i)$ is constructed based on connected components[13]. $V_i = (v_{i1}, v_{i2}, .., v_{im})$ is the node set, where $m$ denotes the number of nodes in $G_i$, $v_{ik}$ $(k = 1, 2, ..., m)$ denotes the $k^{th}$ node. We only consider the connected components with neighbors in graph construction, that is, the number of nodes $m$ is less than or equal to the number of connected components $n$. If two connected components $c_{ip}$ and $c_{iq}$ $(p, q \in [1, n])$ are adjacent to each other, there is an edge $e_{ik} = (v_{ip}, v_{iq})$ $(k \in [1, s])$ between them, where $s$ is the number of edges.

*3) Graph measurements:* Using the region adjacency graph $G_i$ for subject $i$, graph measurements $F_i = (F_i^{general}, F_i^{embedding})$ are extracted, where $F_i^{general}$ denotes the basic graph measurements and $F_i^{embedding}$ denotes the feature vector from graph embedding.

- For $F_i^{general}$, general graph measurements are obtained [14], including nodes, edges, and degree information (Table I).
- To obtain $F_i^{embedding}$, graph embedding is computed for each graph with GL2Vec [15], [16]. This embedding approach preserves the structural information and adds the embeddings of the line graphs. Each graph is now represented by a 128-dimensional feature vector $f_{GE}$. In order to reduce the dimension of the feature vector, we use principal component analysis (PCA) [17] and extract 10 principal components from the graph features.

TABLE I

GENERAL GRAPH FEATURES

| Features | Description |
|---|---|
| Nodes | Number of nodes |
| Edges | Number of edges |
| Degree_number | Number of nodes whose degree is larger than 2 |
| Degree_mode | The mode of node degree |
| Degree_max | The maximum degree value of nodes whose degree is larger than 2 |
| Degree_min | The minimum degree value of nodes whose degree is larger than 2 |
| Degree_avg | The average degree value of nodes whose degree is larger than 2 |

*4) Survival Modeling:* The computed features are used in a Cox proportional-hazards model with clinical parameters such as age and volume to evaluate their prognostic ability. In the Cox model [18], the hazard function is defined as $\lambda(t|x) = \lambda_0(t)e^{h(x)}$, where $t$ is the time, $x$ is feature vector, $\lambda_0(t)$ denotes the baseline hazard function, $h(x)$ is the risk function. The Cox model utilizes the partial likelihood $L_c(\beta) = \prod_{i:E_i=1} \frac{exp(\hat{h}_\beta(x_i))}{\sum_{j \in R(T_i)} exp(\hat{h}_\beta(x_j))}$ to find the weights $\beta$ and compute $\hat{h}_\beta(x) = \beta^T x$, where $T_i$ is the event time, $E_i$ is the event indicator, $x_i$ is the baseline data for subject $i$, and risk set $R(t) = \{i : T_i >= t\}$ is risk subject set at time $t$ [19]. The Risk score is defined as the partial hazard $RiskScore = e^{h_\beta(x)}$[20].

We performed a 5-fold cross validation on the dataset for 10 iterations with a Cox model including both an L1 and L2 penalty [20]. Two risk groups are identified according to the median risk score determined on the training folds. Majority voting was used to assign each patient into either the low-risk or the high-risk category.

*5) Radiomic model:* As a comparative strategy, 1320 textural radiomic features such as shape, gray level run length, gray level co-occurrence matrix, and neighboring gray tone difference matrix features were extracted from each of the global tumor habitats using PyRadiomics [21]. Recursive feature elimination is utilized with a decision tree regressor to select 45 radiomic features.

## III. Results

Experiment results including concordance-index (C-index) and hazard ratios (HR) between the two risk groups (high risk group and low risk group) are shown in Table II. The average and standard deviation values of C-index across ten iterations are provided.

**Baseline Model 1.** We use $age$ and $Volume_i$ as features (referred to as $Clinical\ features$ in the tables) in our baseline model 1 to train a Cox proportional hazards model. **Baseline Model 2.** We use radiomic features, $age$ and $Volume_i$ as features in our baseline model 2 to train a Cox proportional hazards model.
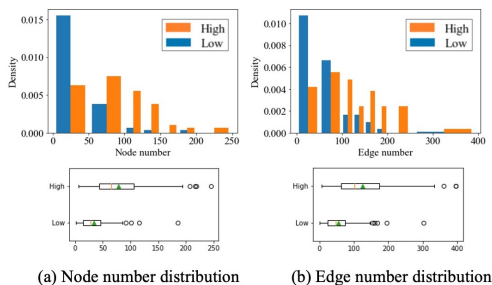


Fig. 2.    Graph comparison between two risk groups

**Prognostic model using global graph features.** In the first experiment, we used global graph features $F_i$, along with $age$ and $Volume_i$ as the prognostic factors. As shown in Table
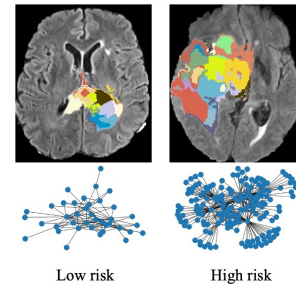


Fig. 3.    Examples of 3D graphs from local FLAIR habitats

TABLE II
SURVIVAL METRICS USING DIFFERENT FEATURES

| Experiment | Features | Survival Metrics |
|---|---|---|
| Baseline 1 | Clinical features | C-index: 0.6401±0.0069 HR: 1.7354 (1.3311, 2.2624) |
| Baseline 2 | Clinical features Radiomic features | C-index: 0.6367±0.0200 HR: 1.9122 (1.4581, 2.5077) |
| 1 | Clinical features Global graph features | **C-index: 0.6624±0.0036 HR: 2.1967 (1.6619, 2.9035)** |
| 2 | Clinical features Local graph features (FLAIR) | **C-index: 0.6503±0.0080 HR: 1.8182 (1.3895, 2.3793)** |
| 3 | Clinical features Local graph features (T1) | C-index: 0.6482±0.0077 HR: 1.8324 (1.4018, 2.3952) |
| 4 | Clinical features Local graph features (T2) | C-index: 0.6480±0.0053 HR: 1.9799 (1.5119, 2.5927) |
| 5 | Clinical features Local graph features (T1-Gd) | C-index: 0.6428±0.0084 HR: 1.6135 (1.2371, 2.1044) |

II (experiment 1), adding the global graph features improved the C-index to 0.6624 from 0.6401 in the Cox model. HR also improved to 2.1967 from 1.7354. After cross-validated assignment of each patient into different risk groups, we compared the distribution of the number of nodes $m$ and the number of edges $s$ per patient in the two groups. Figure 2 shows a clear difference in the feature distribution across the two risk groups. Additionally, there was a significant difference in the node number and the edge number between the different risk groups ($p < 0.05$).

**Prognostic model using local graph features.** In experiments 2-5, we leveraged the local graph features from all protocols, $age$ and $Volume_i$ in the Cox model. The C-indices for each of the four protocols (Table II) showed an improvement over the baseline using just clinical features. The HR values using the T1, T2, and FLAIR local habitat features also showed an improvement from 1.7354 to 1.8324,
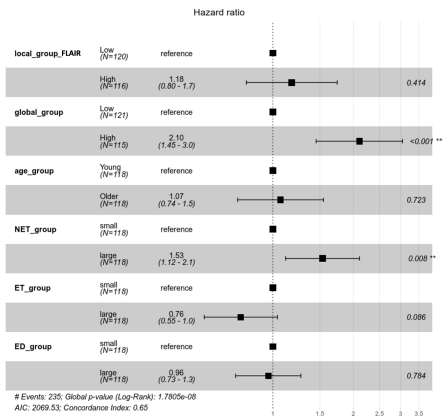
Fig. 4. Multivariable Cox analysis with different risk groups

1.9799, and 1.8182, respectively. The local habitats from FLAIR protocol, in conjunction with the *clinical features*, yielded the highest C-index. However, the HR was higher using the T2 local habitat features. All the protocols except T1-Gd showed an improvement in HR compared to baseline HR of 1.7354. Figure 3 shows examples of local habitats and associated 3D graphs from representative scans from the two different risk groups. Similar to global graphs, the local habitat graphs were found to be denser for the high risk cases. In order to estimate the independent prognostic ability of global and local habitats in a multivariable setting, the risk groups from both the local and the global habitat features and the clinical information are provided to another Cox model as independent variables. The global risk group showed a HR of 2.1 in the multivariable setting which is significantly higher than the reference. As seen in the forest plot (Figure 4), the $NET_i, ET_i, ED_i$ are divided into two groups based on the median value of each volume, yielding $NET\_group, ET\_group, ED\_group$, respectively. Also, two groups are obtained using the median age. The risk groups from global habitats and NET both showed significant contributions to the survival prediction. Interestingly, the local habitat features were not significantly prognostic in this setting.

**Comparison with radiomics.** Both C-indices and HR using the radiomic + clinical features were lower when compared to survival model using global habitat + clinical features. Though local graph features yielded higher C-indices, the HR for the radiomic features were higher than those for the local graph features from T1, FLAIR, and T1-Gd sequences. Compared to the baseline model, when we added the graph features from global habitats and local habitats in experiments 1-5, the C-indices showed an improvement, outperforming the radiomic features. The HR using global graph features is also higher than the HR using the radiomic descriptors. Though the global habitat signatures are more prognostic, the local habitat features provide a more comprehensive protocol-specific characterization.

## IV. CONCLUSION

Ecological analysis of tumor phenotypes via radiologically defined habitats can provide valuable prognostic and pre-

dictive information in cancer. Our results seem to suggest that the inner structural diversity of GBMs can be quantified by spatial analysis of radiologically-defined local and global habitats. In future work, we propose to design and evaluate prognostic graph neural networks leveraging the constructed 3D graphs from local and global habitats.

## V. COMPLIANCE WITH ETHICAL STANDARDS

This research study was conducted retrospectively using open access human subject data (BraTS 2020). Additional approval was not required as confirmed by the license attached with the dataset [9], [10], [11].

## REFERENCES

[1] Krex, D. et al. Long-term survival with glioblastoma multiforme. *Brain*, 09 2007.
[2] Bonavia, R. et al. Tumor heterogeneity is an active process maintained by a mutant egfr-induced cytokine circuit in glioblastoma. *Genes & development*, 2010.
[3] Prasanna, Prateek, et al. Radiomic features from the peritumoral brain parenchyma on treatment-naive multi-parametric MR imaging predict long versus short-term survival in glioblastoma multiforme: preliminary findings. *European radiology,* 2017.
[4] Zhou, M. et al. Radiologically defined ecological dynamics and clinical outcomes in glioblastoma multiforme: preliminary results. *Translational oncology*, 2014.
[5] Otsu, Nobuyuki. A threshold selection method from gray-level histograms. *IEEE transactions on systems, man, and cybernetics* 9.1 (1979): 62-66.
[6] Jia Wu et al. Tumor subregion evolution-based imaging features to assess early response and predict prognosis in oropharyngeal cancer. *Journal of Nuclear Medicine*,2020.
[7] Stefania Rizzo et al. Radiomics: the facts and the challenges of image analysis. *European radiology experimental*, 2(1):1–8, 2018.
[8] Stefania Rizzo et al. Radiomics: the facts and the challenges of image analysis. *European radiology experimental*, 2(1):1–8, 2018.
[9] Bjoern H Menze et al. The multimodal brain tumor image segmentation benchmark (brats). *IEEE transactions on medical imaging*, 34(10):1993–2024, 2014.
[10] Spyridon Bakas et al. Advancing the cancer genome atlas glioma mri collections with expert segmentation labels and radiomic features. *Scientific data*, 4:170117, 2017.
[11] Spyridon Bakas et al. Identifying the best machine learning algorithms for brain tumor segmentation, progression assessment, and overall survival prediction in the brats challenge. *arXiv preprint arXiv:1811.02629*, 2018.
[12] Benjamin Irving. maskslic: regional superpixel generation with application to local pathology characterisation in medical images. *arXiv preprint arXiv:1606.09518*, 2016.
[13] William-silversmith and Nico Kemnitz. Connected components 3d. Website, 2018. https://github.com/seung-lab/connected-components-3d.
[14] Daniel Kaslovsky. Graphrole. Website, 2018. https://github.com/dkaslovsky/GraphRole.
[15] Hong Chen and Hisashi Koga. Gl2vec: Graph embedding enriched by line graphs with edge features. In *International Conference on Neural Information Processing*, pages 3–14. Springer, 2019.
[16] Benedek Rozemberczki, Oliver Kiss, and Rik Sarkar. Karate Club: An API Oriented Open-source Python Framework for Unsupervised Learning on Graphs. In *arXiv preprint arXiv:2003.04819*. 2020.
[17] Svante Wold et al. Principal component analysis. *Chemometrics and intelligent laboratory systems*, 2(1-3):37–52, 1987.
[18] David R Cox. Regression models and life-tables. *Journal of the Royal Statistical Society: Series B (Methodological)*, 34(2):187–202, 1972.
[19] Jared L Katzman et al. Deepsurv: personalized treatment recommender system using a cox proportional hazards deep neural network. *BMC medical research methodology*, 18(1):24, 2018.
[20] Davidson-Pilon et al. Camdavidsonpilon/lifelines: v0.25.5, 2020.
[21] Joost JM Van Griethuysen et al. Computational radiomics system to decode the radiographic phenotype. *Cancer research*, 77(21):e104–e107, 2017.